PHYSICAL REVIEW E **105**, 025302 (2022)

Reconstruction of three-dimensional objects in layered composite structures from multimode orbital angular momentum

Bingyang Liang,[1,2] Fei Shen,[1,*] Shao meng Wang,[2] Yuanguo Zhou,[3] Yang Yang,[1] Kaiyang Cheng,[1] Guangmin Zhang,[4] Yu Zheng,[4] Qing Huo Liu,[5] and Yubin Gong[1,2,†]

[1] *International School of Microelectronics, Dongguan University of Technology, Dongguan 523808, China*
[2] *National Key Laboratory on Vacuum Electronics, University of Electronic Science and Technology of China (UESTC), Chengdu 610054, China*
[3] *College of Communication and Information Engineering, Xi'an University of Science and Technology, Xi'an 710054, China*
[4] *School of Environment and Civil Engineering, Dongguan University of Technology, Dongguan 523808, China*
[5] *Department of Electrical and Computer Engineering, Duke University, Durham, North Carolina 27708, USA*

(Received 3 November 2021; accepted 13 January 2022; published 4 February 2022)

Because of helical phase wavefront distribution, vortex electromagnetic waves are considered to carry more information and additional degrees of freedom than traditional spherical waves. Therefore, a vortex wave carrying orbital angular momentum (OAM) can improve inversion and imaging accuracy. In this work, we revisit the reconstruction of three-dimensional objects in layered composite structures extended with OAM. In forward modeling, the concentric uniform circle array is used to generate electromagnetic vortex beams. To analyze the difference of vortex beams, the electric field radiation pattern and phase pattern distribution of OAM waves with different modes are calculated. Then, the scattered field of layered media illuminated by different OAM beams is determined by the dyadic Green's function and the stabilized biconjugate gradient technique with a fast Fourier transform algorithm. In the inversion, the variational Born iterative method is used to reconstruct targets in layered composite structures, and multiple OAM modes are used to improve the reconstruction results. The numerical results prove that the permittivity of the target can be better reconstructed by using the multiple OAM modes rather than the traditional spherical wave. With the increase of OAM mode number, the reconstructed target parameters are closer to the true value. We expect that our results will provide a better understanding of the OAM and pave the way for the improvement of inversion and optical imaging technology using vortex waves.

DOI: 10.1103/PhysRevE.105.025302

I. INTRODUCTION

Despite the fact that electromagnetic theory has been developed for more than a century, one property of the electromagnetic field, orbital angular momentum (OAM), was not discovered and verified until 1992 [1–3]. The realization of OAM brought a new understanding of electromagnetics and quickly attracted the attention of researchers. Due to the helicoidal phase profile and mutually orthogonal OAM modes, the vortex electromagnetic wave showed great potential for many fields. These applications range from super-resolution imaging [4,5], optical capture [6], optical manipulation [7], quantum experiments [8,9], and communication expansion [10–12], to SAR imaging [13,14], etc.

The main characteristic of the OAM beams is the helical phase front, and different modes are orthogonal to each other [15]. With the orthogonal OAM modes, the OAM beams can provide new degrees of freedom compared to traditional beams. Therefore, the vortex electromagnetic wave carrying the OAM has the potential to improve the resolution of radar imaging. Guo *et al.* indicated that electromagnetic vortex waves could improve the azimuth resolution of radar targets [16]. Yuan's group designed an imaging system and successfully realized the imaging experiment using vortex electromagnetic waves [17]. The Liu group's long-term research on vortex wave radar imaging showed that vortex electromagnetic waves carrying OAM could improve the radar's target detection ability [18] and antinoise ability [19,20], and even achieve super-resolution imaging [4]. These studies lay the foundation for the application of vortex waves at the field of radar imaging.

In addition, the additional information of the OAM beam can also improve the inversion accuracy. When multiple modes of vortex waves illuminate the target, the scattered fields in the space contain more target information. Li *et al.* proposed a super-resolution imaging method based on orbital angular momentum diffraction tomography (OAM DT), which achieved an important breakthrough in the Rayleigh limit of traditional diffraction tomography (DT) technology [21]. Chen *et al.* used the concept of the OAM carrier to carry out single-frequency microwave imaging and proposed a kind of computational reconstruction method of single-frequency OAM mode [22]. Fan *et al.* proposed a super-resolution imaging method suitable for high-contrast targets [5]. However, these methods mainly aimed at the inversion problem in uniform space. For more complex target detection problems as

---

[*] shenfei@dgut.edu.cn
[†] ybgong@uestc.edu.cn

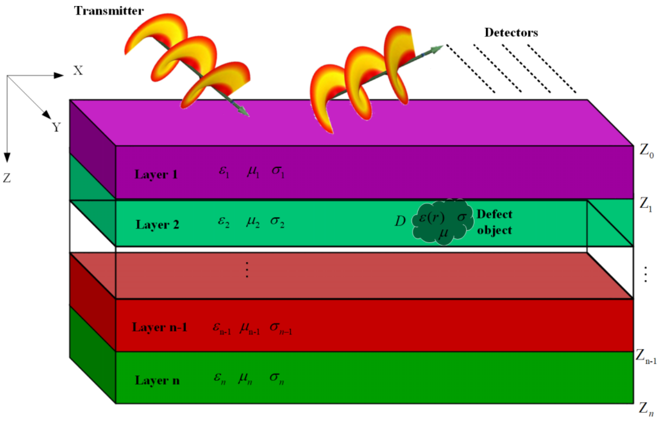

FIG. 1. The typical configuration of 3D inverse scattering problem with an anomaly in the layered medium. The defect area D is embedded in an arbitrary layer. The transmitter emits a vortex electromagnetic wave to irradiate the layered medium; the detectors are arranged in an array on the same side of the transmitter.

in stratified media, due to the complex structure of the model, more information is needed to improve the accuracy of the inversion. The OAM beams are convenient for this.

In this paper, we revisit the three-dimensional (3D) electromagnetic scattering problem of layered composite structures extended with OAM. First, we present the numerical study of vortex waves and the forward theory in Sec. II, especially the generation of different modes of OAM. Then the detailed inversion procedure is demonstrated in Sec. III. Finally, in Sec. IV, a series of numerical experiments is presented to verify the proposed method.

II. THREE-DIMENSIONAL FORWARD MODELING OF VORTEX WAVE

In this section, we derive the electromagnetic fields in a layered model excited by vortex waves of different OAM beams, and calculate the scattering fields of three-dimensional inhomogeneous scatterers embedded in an arbitrary layer.

A. Modeling

The typical configuration of the electromagnetic scattering problem in a layered composite structure is depicted in Fig. 1, where the defect object is inhomogeneous, while the background is a homogeneous planar layered medium. The planar layer interfaces extending to infinity in both the X and Y directions, and perpendicular to the Z direction. Each layer is a kind of homogeneous medium with a permittivity of ε_n, a permeability of μ_n, and a conductivity of σ_n ($n = 1, \ldots, N$). The abnormal area D is embedded in an arbitrary layer, with the permittivity of $\varepsilon(r)$, permeability of μ, and conductivity of σ. The transmitter emits a vortex electromagnetic wave to irradiate the layered medium.

B. OAM beam excitation

The vortex electromagnetic wave can be equivalent to the superposition of waves with different phases at different angles to a certain extent. There are many methods of generating a vortex beam carrying the OAM, such as a helicoidal parabolic antenna [23], spiral phase plates [24,25], computer-aided holograms [26,27], uniform circular array (UCA) [15,28,29], circular polarized patch antenna [30], time switch array antenna [31], and so on [32]. As the UCA method can generate arbitrarily OAM beams flexibly, in this article, a typical M-element circular phased array is used to generate vortex beams, as shown in Fig. 2.

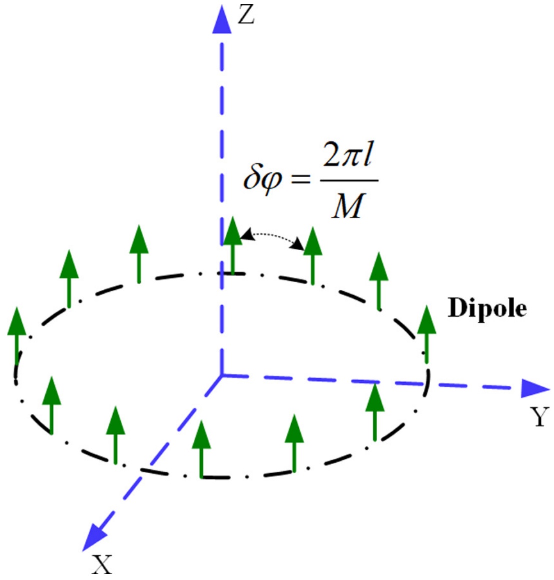

FIG. 2. The geometries of the circular antenna array used for OAM modes.

The circular array is composed of M electric dipoles evenly distributed on the circumference. The phase difference between each two adjacent elements is $\varphi = 2\pi l/M$ (M is the number of array elements, l is the OAM mode, $l < M/2$) [33]. In a homogeneous medium, the spatial radiation of the m element can be expressed as [4,19]

$$\boldsymbol{E}_m(\boldsymbol{r'}, \varphi) = \frac{A(\boldsymbol{r'})e^{j[(m-1)\varphi + k|\boldsymbol{r}-\boldsymbol{r}'_m|]}}{|\boldsymbol{r} - \boldsymbol{r}'_m|}, \tag{1}$$

where $A(r')$ is the intensity of the antenna emission, k is the wave number of the space, l represents the OAM mode number, and $\boldsymbol{r'} = (x', y', z')$ and $\boldsymbol{r} = (x, y, z)$ represent the position vector of the source point and the field point, respectively. For the circle array emission source, its spatial radiation can be expressed as

$$\boldsymbol{E}_O(\boldsymbol{r'}, \varphi) = \sum_{m=1}^{M} A(r')e^{j[(m-1)\varphi + k|\boldsymbol{r}-\boldsymbol{r}'_m|]}, \tag{2}$$

where $\boldsymbol{E}_O$ represents the electric field component of the vortex wave.

The local behavior of OAM beams in a homogeneous medium is shown in Fig. 3. The intensity and phase distribution of the spatial radiation are different from the same site with different modes due to the emission phase of the array antenna. The spiral wavefront phase distribution grows outward along the Z axis as a result of radiation [Figs. 3(b) and 3(d)]. More degrees of freedom are provided by these distinct

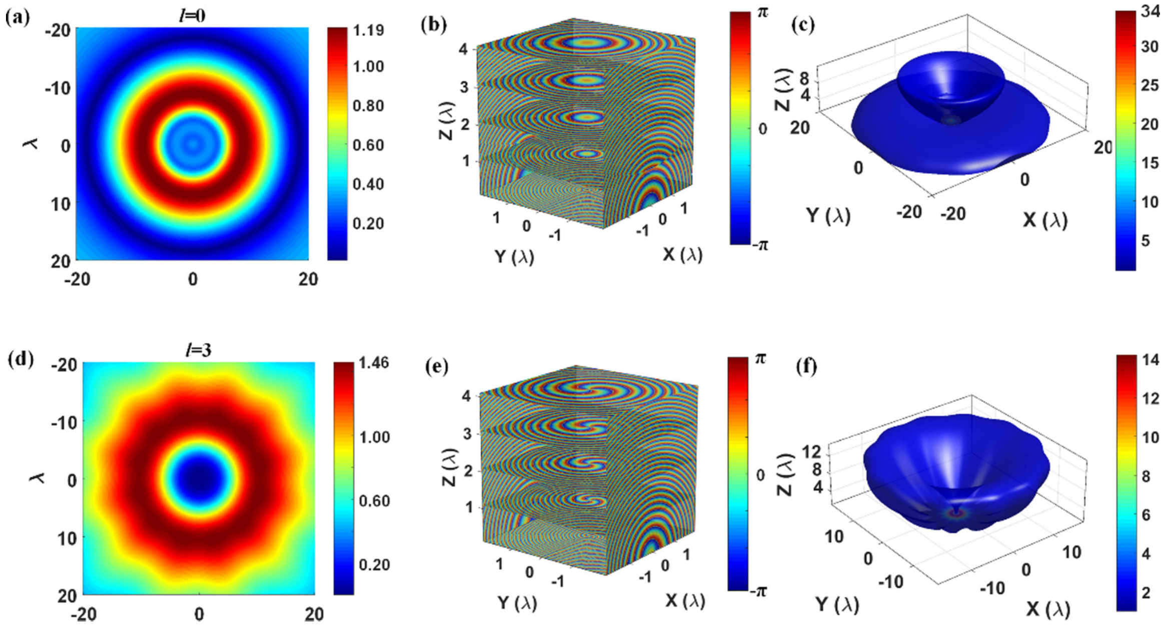

FIG. 3. The local behavior of Ez radiated, from a 12-element circular OAM-generating array with diameter $D = \lambda$, at $f = 30\,\mathrm{GHz}$. The upper row is the radiation behavior of $l = 0$: (a) a transverse plane at z = 10λ; (b) 3D phase patterns; (c) 3D electric density patterns. The bottom row is the radiation behavior of $l = 3$: (d) a transverse plane at $z = 10\lambda$; (e) 3D phase patterns; (f) 3D electric density patterns.

spatial radiations and spatial phase information, which may increase inversion accuracy.

C. Forward modeling

According to the electromagnetic scattering theory [34–36], the total field $\boldsymbol{E}^{\mathrm{tot}}$ is the sum of the incident field $\boldsymbol{E}^{\mathrm{inc}}$ and scattered field $\boldsymbol{E}^{\mathrm{sct}}$:

$$\boldsymbol{E}^{\mathrm{tot}}(\boldsymbol{r}) = \boldsymbol{E}^{\mathrm{inc}}(\boldsymbol{r}) + \boldsymbol{E}^{\mathrm{sct}}(\boldsymbol{r}), \tag{3}$$

where $\boldsymbol{E}^{\mathrm{inc}}$ represents the three directions' incident electric field in the absence of the targets. The incident wave field $\boldsymbol{E}^{\mathrm{inc}}$ carrying OAM mode can be expressed as

$$\boldsymbol{E}^{\mathrm{inc}}(\boldsymbol{r}) = \int \bar{\bar{\boldsymbol{G}}}(\boldsymbol{r}, \boldsymbol{r}')\boldsymbol{J}_{ol}(\boldsymbol{r}', \varphi)d\boldsymbol{r}', \tag{4}$$

where $\bar{\bar{\boldsymbol{G}}}(r, r')$ is the dyadic Green's functions (DGF) of the layered medium [37], $\boldsymbol{J}_{ol}(r', \varphi)$ denotes the vortex wave source with mode 1 excited by N circle array, $\boldsymbol{J}_{ol}(\boldsymbol{r}', \varphi) = \sum_{m=1}^{M} \boldsymbol{A}(\boldsymbol{r}')e^{l(m-1)\varphi}$. If the DGF for the electric field $\boldsymbol{E}^{\mathrm{inc}}$ is adopted, the scattered electric field can be written more compactly as

$$\boldsymbol{E}^{\mathrm{sct}}(\boldsymbol{r}) = j\omega\mu_b \int_D \bar{\bar{\boldsymbol{G}}}(\boldsymbol{r}, \boldsymbol{r}')\bar{\bar{\chi}}_\varepsilon(\boldsymbol{r}')\boldsymbol{D}^{\mathrm{tot}}(\boldsymbol{r}')d\boldsymbol{r}', \tag{5}$$

where $\bar{\bar{\chi}}_\varepsilon$ is the dielectric contrast function defined as $\bar{\bar{\chi}}_\varepsilon = \frac{\tilde{\boldsymbol{\varepsilon}}(r) - \tilde{\boldsymbol{\varepsilon}}_b}{\tilde{\boldsymbol{\varepsilon}}(r)}$; $\boldsymbol{D}^{\mathrm{tot}} = \tilde{\varepsilon}\boldsymbol{E}$ is the electric flux density; and $\tilde{\varepsilon}_b$ is the complex permittivity of the scattering layer. Substituting Eqs. (3) and (4) into (5) yields

$$\boldsymbol{E}^{\mathrm{inc}}(\boldsymbol{r}) = \tilde{\varepsilon}^{-1}(\boldsymbol{r})\frac{\boldsymbol{D}^{\mathrm{tot}}(\boldsymbol{r})}{\varepsilon} - j\omega \int_D \bar{\bar{\boldsymbol{G}}}(\boldsymbol{r}, \boldsymbol{r}')\bar{\bar{\chi}}(r')\boldsymbol{D}^{\mathrm{tot}}(\boldsymbol{r}')d\boldsymbol{r}'. \tag{6}$$

A linear system is obtained by using Galerkin's method to discretize Eq. (6). The total electric field flux $\boldsymbol{D}^{\mathrm{tot}}$ is obtained by solving the above equation using the stabilized biconjugate gradient fast Fourier transform (BCGS FFT) method [38,39]. Once the total field is obtained, the scattering field distribution in space can be obtained according to Eq. (5).

III. INVERSION METHODOLOGY

In the inversion procedure, the scattered field $\boldsymbol{E}^{\mathrm{sct}}$ in the space can be measured by the detector; the permittivity of the inversion region needs to be calculated [34,40]. The relationship between the scattering field and the medium in the space can be expressed as

$$\delta\boldsymbol{E}^{\mathrm{sca}}(\boldsymbol{r}, \boldsymbol{r}') = j\omega \int_D \bar{\bar{\boldsymbol{G}}}^{\boldsymbol{HJ}}(\boldsymbol{r}, \boldsymbol{r}')\delta\bar{\bar{\chi}}_\varepsilon(\boldsymbol{r}')\boldsymbol{D}^{\mathrm{tot}}(\boldsymbol{r}')d\boldsymbol{r}',$$
$$\boldsymbol{r} \in \boldsymbol{D}_{\mathrm{obs}}, \quad \boldsymbol{r}' \in \boldsymbol{D}_{\mathrm{inv}}. \tag{7}$$

Simplify to

$$\delta\boldsymbol{E}^{\mathrm{sct}}(\boldsymbol{r}) = \boldsymbol{E}^{\mathrm{sct}(n+1)}(\boldsymbol{r}) - \boldsymbol{E}^{\mathrm{sct}(n)}(\boldsymbol{r}) = \boldsymbol{M}\delta\bar{\bar{\chi}}_\varepsilon^n, \tag{8}$$

where $\delta\boldsymbol{E}^{\mathrm{sct}}$ represents the difference between the measured scattered field and the predicted scattered field in the nth iteration step. In the inverse problem, assuming that there are M_t transmitters and M_r receivers and nf frequencies are used, the inversion area is discretized into $N_x \times N_y \times N_z$ small voxels. The size of the $\boldsymbol{M}$ matrix is $M_c \times N_c$ ($M_c = M_r \times M_t \times nf$, $N_c = N_x \times N_y \times N_z$). By employing the Tikhonov regularization technology, the normalized cost functional during iteration can be defined as [41,42]

$$\boldsymbol{F}(\delta\chi) = \frac{\left\|\delta\boldsymbol{E}_n^{\mathrm{sct}} - \boldsymbol{M}_n\delta\bar{\bar{\chi}}_n\right\|^2}{\|\delta\boldsymbol{L}_n\|^2} + \gamma^2\frac{\|\delta\bar{\bar{\chi}}_{n+1}\|^2}{\|\delta\bar{\bar{\chi}}_n\|^2}, \tag{9}$$

where $\|\centerdot\|$ denotes the $L2$ norm and γ is the regularization parameter, The subscripts n and $n+1$ in the formula represent the result of the nth and $(n+1)$th iteration. The minimization

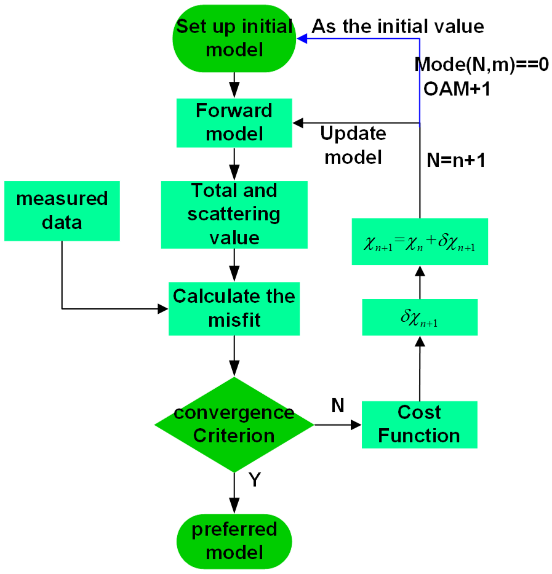

FIG. 4. The flow chart of the inverse procedure.

of the cost function is equivalent to solving the following equation:

$$\left(\boldsymbol{M}_n^T\boldsymbol{M}_n+\gamma^2\frac{\delta\boldsymbol{E}_n^{\mathrm{sct}}}{\delta\bar{\bar{\chi}}_\varepsilon^n}I\right)\delta\bar{\bar{\chi}}_{n+1}=\boldsymbol{M}_n^T\delta\boldsymbol{E}_n^{\mathrm{sct}}, \qquad (10)$$

where the superscript T denotes the conjugate transpose. The equation can be solved effectively by the matrix solving method, such as conjugate gradient (CG), matrix decomposition, and so on. Due to the limited effective information obtained from the measured data, Eq. (10) has multiple solutions and an ill-posed problem. If we can increase the effective information in the process of solving, the accuracy of the inverse problem can be improved.

The iterative process of inversion is shown in Fig. 4. Firstly, set the initial value of the model, and calculate the total field and scattered field using the BCGS FFT method [34]. Secondly, calculate the misfit between measured data and the model scattered data; if the data error is greater than the threshold, the cost function and the contrast function are calculated. Once the $\delta\chi_{n+1}$ is obtained, the contrast function is updated immediately, and the new model will be obtained. At this time, if the iteration numbers of each mode exceed m, the new OAM mode is used for the next iteration. The iteration continues until the convergence condition is satisfied. The model that satisfies the convergence condition and the minimum error is the preferred model.

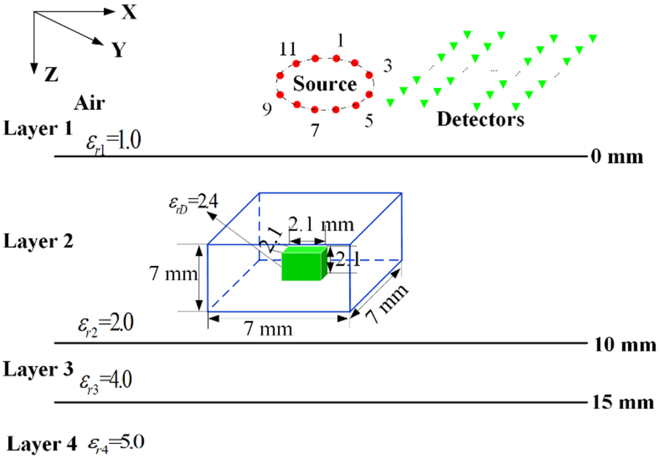

FIG. 5. The configuration of the inversion model with the layered medium. The target model is located on the second layer. The blue cubic block denotes forward computational domain. Green cubic block denotes scattering object.

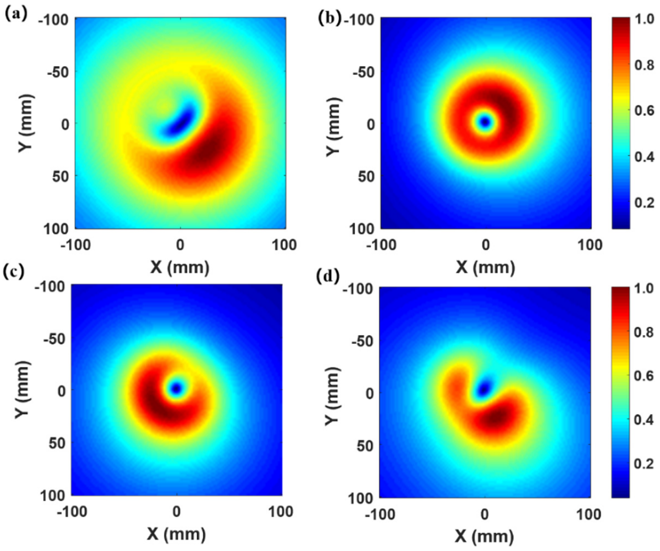

FIG. 6. The scattered fields of *Ez* radiated over a transverse plane at $z=-30$ mm, at the frequency $f=30$ GHz. (a) The OAM mode $l=0$; (b) the OAM mode $l=1$; (c) the OAM mode $l=3$; (d) the OAM mode $l=5$.

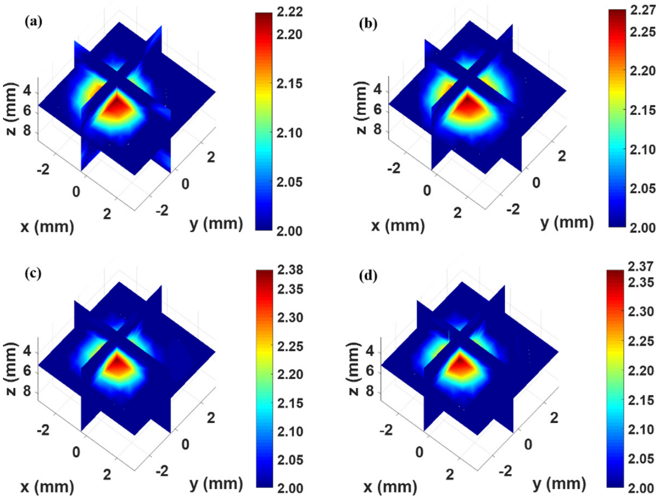

FIG. 7. Reconstructed relative permittivity of the cube. (a) The 3D result using the classical electromagnetic wave ($l=0$); (b) the 3D result using one OAM beam ($l=1$). (c) The 3D result using *three* modes of vortex waves ($l=1, 2, 3$). (d) The 3D result using *five* modes of vortex waves ($l=1, 2, 3, 4, 5$).

TABLE I. The details of model 1 reconstruction results.

OAM mode number	1 ($l = 0$)	1 ($l = 1$)	3 ($l = 1, 2, 3$)	5 ($l = 1, 2, 3, 4, 5$)	True model
Maximum reconstruction result	2.221	2.277	2.382	2.369	2.400
Number of voxels greater than 2.15	8	23	29	27	27

IV. NUMERICAL RESULTS

In this section, four different detection system configuration scenarios are designed to verify the OAM beam inversion. The inversion results using the point source, traditional electromagnetic, and different OAM beams are obtained.

In the first scenario, the configuration of the inversion model for nondestructive testing is shown in Fig. 5. The model has four layers: The first layer is air with a relative permittivity of 1.0; the relative permittivity of the second and second layers are $\varepsilon_{r2} = 2.0$, $\varepsilon_{r3} = 4.0$ and the thicknesses are 10 and 5 mm, respectively; the fourth layer extends downward to infinity and the relative permittivity is $\varepsilon_{r4} = 5.0$. The conductivity and permeability of the layered media are $\sigma = 0.001$ s/m and $\mu_r = 1$. The scatterer is embedded in the second layer, and the relative permittivity is 2.4. The vortex waves of different OAM modes are generated by 12 circular electric dipole sources distributed among space. The center of the circle is the origin (0, 0, −10) mm. In this work, only one operating frequency, 30 GHz, is adopted.

Due to the different spatial radiation intensities of vortex waves of different modes, when vortex waves at different modes are used to illuminate the target, the scattered field distributions of the space are also different. Figure 6 demonstrates the distributions of scattered field of space under different modes of illumination. When multiple modes are used for inversion, the amount of inversion information increases, so the inversion accuracy can be improved.

According to Eq. (1), different OAM modes can be realized by changing the phase difference between the arrays. The maximum number of modes that the array can produce are less than $M/2$. The detectors are used to collect the scattered fields of the first layer. A total of 121 detectors are evenly distributed over the (−50 mm, −50 mm, −30 mm)–(50 mm, 50 mm, −30 mm). The inversion area is embedded in the second layer with the size of 7 mm × 7 mm × 7 mm and is divided into 10 × 10 × 10 voxels. There is one cube scatterer in the reconstructed region, which is 2.1 mm × 2.1 mm × 2.1 mm (3 × 3× 3 voxels). Figure 7 shows the 3D slices of the retrieved relative permittivity value of the scatterer under different OAM modes. In a personal laptop with a CPU with Intel core i7-7700HQ 2.80 GHz, the inversion takes 215.6, 215.7, 671.4, and 1097.9 s CPU time, respectively. Figures 7(a) and 7(b) illustrate the fact that the result of only one OAM model ($l = 1$) is close to the traditional electromagnetic ($l = 0$) inversion results. As the number of OAM modes increases [Figs. 7(c) and 7(d)], the permittivity of the reconstructed scatter is closer to the true value, 2.4. We also investigated the details of the reconstruction results, as summarized in Table I. As the number of OAM modes increases, the maximum reconstruction result becomes closer and closer to the real value. If we define a voxel with a

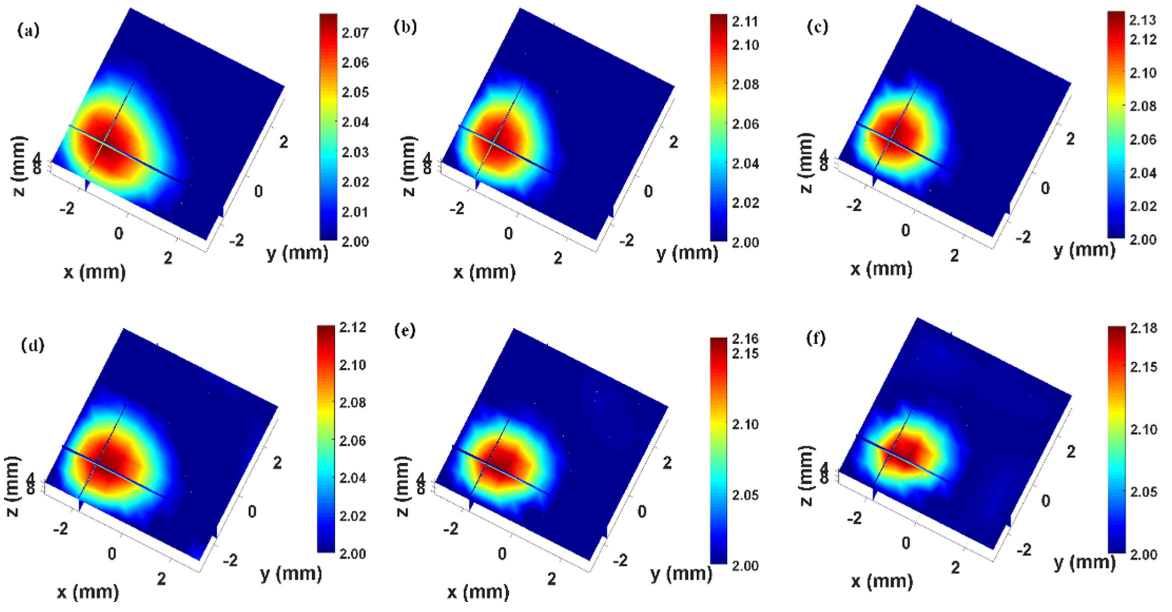

FIG. 8. Reconstructed relative permittivity of the cube using vortex-free wave and vortex wave. The top row (a–c) are reconstructed results by dipole sources, one ($m = 1$), three ($m = 1, 2, 3$), and five ($m = 1, 2, 3, 4, 5$) dipole sources are used, respectively. The bottom row (d–f) are reconstructed results by vortex waves, one ($l = 1$), three ($l = 1, 2, 3$), and five ($l = 1, 2, 3, 4, 5$) vortex modes are used, respectively.

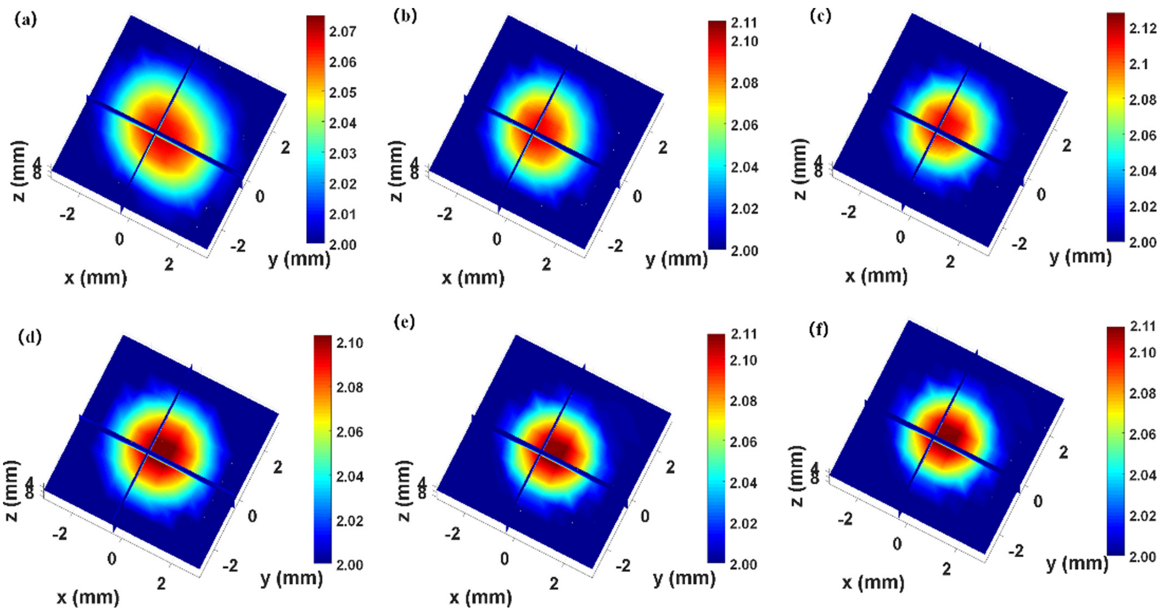

FIG. 9. Reconstructed relative permittivity of the cube using vortex-free wave and vortex wave. The top row (a–c) are reconstructed results by dipole sources, one ($m = 1$), three ($m = 1, 2, 3$), and five ($m = 1, 2, 3, 4, 5$) dipole sources are used, respectively. The bottom row (d–f) are reconstructed results by vortex waves, one ($l = 1$), three ($l = 1, 2, 3$), and five ($l = 1, 2, 3, 4, 5$) vortex modes are used, respectively.

relative permittivity greater than 2.15 as a scatterer, then the reconstruction results using the five modes are consistent with the true value.

In most cases, superpositioning vortex-free modes in multiple orientations improves inversion accuracy. The second scenario is created to demonstrate the differences between various vortex-free and vortex modes. The system setups are the same as in scenario 1, except the cube scatterer is on the left side of the reconstruction region and the array antenna is 1.4 mm × 1.4 mm × 1.4 mm (2 × 2× 2 voxels) in size. A 12-element dipole circular array can also produce several forms of vortex waves. The array's first through fifth dipoles generate a vortex-free wave for ease. The comparison of the reconstructed relative permittivity is shown in Fig. 8. The maximum value of the reconstructed relative permittivity is enhanced with the superposition of emission sources, regardless of whether the wave is vortex free or is a vortex wave. The greatest relative permittivity of the scatterer reconstructed by a vortex wave is 2.18 [Fig. 8(f)], whereas it is only 2.13 when vortex-free waves are used [Fig. 8(c)].

Vortex waves feature a dark core for various OAM radiation types (Fig. 3). The lowest phase angle and amplitude are zero in this area, and the electric field strength is low. The inversion performance will be influenced by these characteristics. As a result, the third scenario is intended to determine the impact of this region on the inversion. The system configurations are the same as scenario 2, and the cube scatterer, with a size of 1.4 mm × 1.4 mm × 1.4 mm (2 × 2× 2 voxels), falls in the dark core, which is placed in the center of the reconstruction region. Figure 10 shows the reconstruction results of relative permittivity between **a** vortex-free wave and a vortex wave. The maximum value of the relative permittivity reconstructed by vortex-free waves increases with the superposition of emission sources [Figs. 9(a)–9(c)], and the reconstructed target area (Red area) changes from ellipse to circle. The rebuilt target area is near to a circle even if just one mode is used [Fig. 9(d)]. This is owing to the large number of components pointing in different directions. The highest value of relative permittivity reconstructed by vortex-free waves, on the other hand, does not alter much [Figs. 9(d)–9(f)]. The greatest value of relative permittivity fell from 2.18 [Fig. 8(f)] to 2.12 [Fig. 9(f)] as compared to the reconstructed outcome in scenario 2. The aforementioned results show that the object is in the black core, that the target can still be reconstructed, and that the reconstructed target shape is more realistic. The maximum value of reconstructed relative permittivity, however, drops due to the low electric and magnetic field intensity in the dark core.

To further verify the effect of OAM beams for inversion, the fourth scenario is designed. In this scenario, only one

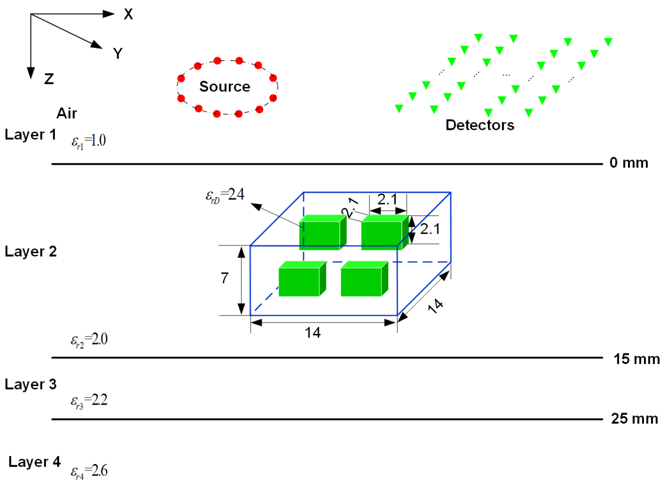

FIG. 10. The configuration of the inversion model with the layered medium. The reconstruction area is the blue box in the figure.

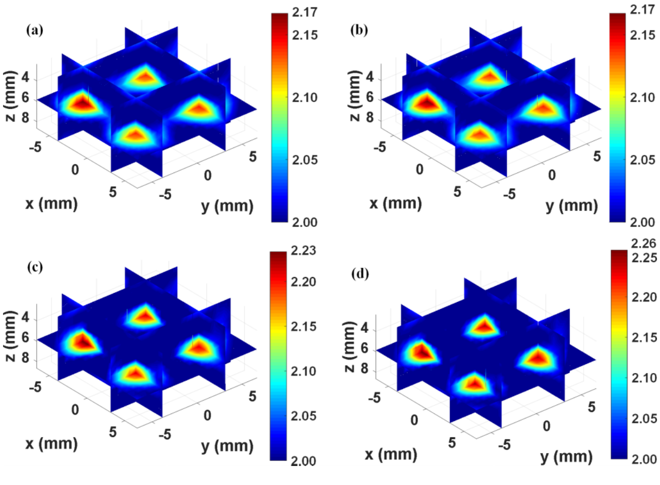

FIG. 11. Reconstructed relative permittivityof the cubes. (a) The 3D result using the classical electromagnetic wave ($l = 0$). (b) the 3D result using one mode ($l = 1$) vortex waves. (c) The 3D result using three modes ($l = 1, 2, 3$) of vortex waves. (d) The 3D result using five modes ($l = 1, 2, 3, 4, 5$) of vortex waves.

operating frequency, 30 GHz, is adopted. The details of the model are shown in Fig. 10. The scatterers are four cubes, with the relative permittivity of 2.4, embedded in the second layer. The vortex waves of different OAM modes are also generated by 12 circular electric dipole sources distributed among space. The center of the circle is the origin (0, 0, −20) mm. The detectors are used to collect the scattered field of the first layer. There are 121 detectors spaced uniformly across the (−7 mm, −7 mm, −10 mm)–(7 mm, 7 mm, −10 mm). The inversion area is embedded in the second layer with the size of 14 mm × 14 mm × 7 mm and divided into 20 × 20 × 10 voxels There are four cube scatterers in the reconstructed region; each scatterer has the same size, which is 2.1 mm × 2.1 mm × 2.1 mm (about $0.3\lambda \times 0.3\lambda \times 0.3\lambda$). The relative permittivity of the four cube scatterers are $\varepsilon_r = 2.4$.

We perform the inversion by the variational Born iterative method (VBIM) with different OAM mode numbers [41–43]. The inversion region's relative permittivity is the same as the backdrop at the start of the iteration. The prescribed threshold of the magnetic field relative error is 0.5%, and the number of iterations in each OAM mode is six. Figure 11 shows the 3D slices of the retrieved relative permittivity value of the scatterers with the OAM mode 0 (classical electromagnetic wave), the OAM mode 1, three OAM modes, and five OAM modes, respectively. The reconstruction results can also reveal the location, size, and relative dielectric constant of the target. As the number of OAM modes increases, reconstructed images become remarkably sharper; in particular the reconstructed relative permittivity value is closer and closer to the true value, 2.4. We also investigated the details of the reconstruction results, as summarized in Table II. This model shows that the inversion results using one mode ($l = 0$ and $l = 1$) are consistent. As the number of OAM modes increases, both the maximum value of inversion results and the number of scatterers are closer to the true value.

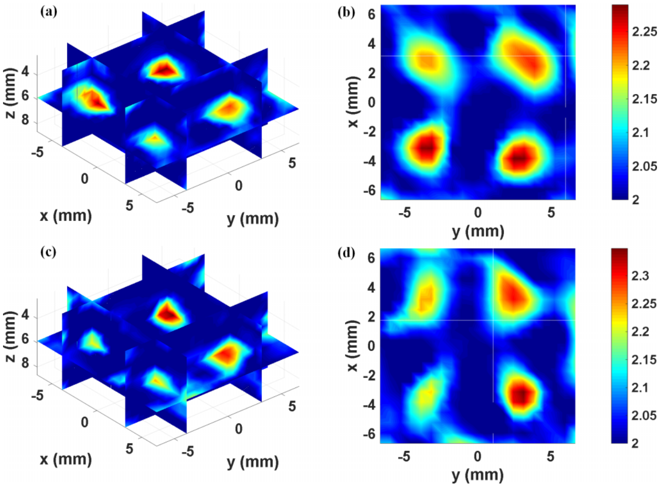

FIG. 12. Reconstructed relative permittivityof the cubes for input data with white Gaussian noise. (a) The 3D result using five modes of vortex waves ($l = 1, 2, 3, 4, 5$) with 5% Gaussian noise. (b) The 2D slice at center of cubes in the z direction. (c) The 3D result using five modes of vortex waves ($l = 1, 2, 3, 4, 5$) with 10% Gaussian noise. (d) The 2D slice at the center of the cubes in the Z direction.

To further investigate the tolerance of the inverse method to the noise, the 3D reconstruction results in the relative permittivity under 5% and 10% random Gaussian noise are calculated and shown in Fig. 12. Figures 12(a) and 12(c) show the 3D slices of the retrieved relative permittivity value of the scatterers with five OAM modes ($l = 1, 2, 3, 4, 5$) under 5% and 10% random noise, respectively. Figures 12(b) and 12(d) are the two-dimensional (2D) slices of Figs. 12(a) and 12(c) with the z cross sections. We observe that the retrieved results are consistent with the model parameters. Four targets can be seen in the reconstruction results under various noise. As the noise increases, the shape, size, and the value of the relative permittivity of the reconstructed object are changed. Even if the noise is increased to 10%, the algorithm can still reconstruct four targets. The results show that the inversion algorithm has a certain antinoise ability. The above scenarios collectively indicate that the inversion result will be improved as the number of OAM modes increases.

TABLE II. The details of model 2 reconstruction results.

OAM mode number	1 ($l = 0$)	1 ($l = 1$)	3 (l = 1, 2, 3)	5 (l = 1, 2, 3, 4, 5)	True model
Maximum reconstruction result	2.167	2.167	2.233	2.257	2.400
Number of voxels greater than 2.15	5	5	55	80	108

V. CONCLUSION

In this work, the vortex electromagnetic wave carrying OAM is combined with the VBIM method to realize the three-dimensional reconstruction of the layered medium. The BCGS FFT method is used to solve the scattering field of the targets. The VBIM method is used to reconstruct the permittivity of the targets. The results of numerical simulation showed that just one mode was performed for inversion; the amount of additional information was limited. Currently, the inversion results using one OAM beam were very close to the traditional electromagnetic wave inversion results. When the number of OAM modes increases, the inversion results will become better. It is necessary to emphasize that compared the influence of different OAM modes, only one frequency of data is used in this paper. Further, we can improve the reconstruction results by adding frequency data for better outcomes. The OAM beams provide a path of more accurate inversion, which will also provide an alternative path of optical imaging. Next, using experiments to verify the theoretical results will be an important step.

ACKNOWLEDGMENTS

The authors acknowledge the Guangdong-Dongguan joint fund (Grants No. 2020A1515110600 and No. 2021B1515140049); Equipment Advance Research Grant No. 80916010504, Natural Science Basic Research Program of Shanxi “Research and Development” (Grant No. 2021JQ-573), and the National Natural Science Foundation of China (Grants No. 61921002 and No. 61988102).

[1] J. H. Poynting, Proc. R. Soc. London, Ser. A **82**, 560 (1909).
[2] R. A. Beth, Phys. Rev. **50**, 115 (1936).
[3] L. Allen, M. W. Beijersbergen, R. J. C. Spreeuw, and J. P. Woerdman, Phys. Rev. A **45**, 8185 (1992).
[4] K. Liu, Y. Cheng, Y. Gao, X. Li, Y. Qin, and H. Wang, Appl. Phys. Lett. **110**, 164102 (2017).
[5] Q. M. Fan and C. Y. Yin, Acta Physica Sinica-Chinese Edition **67**, 144101 (2018).
[6] A. M. Yao and M. J. Padgett, Adv. Opt. Photonics **3**, 161 (2011).
[7] K. C. Neuman and S. M. Block, Rev. Sci. Instrum. **75**, 2787 (2004).
[8] M. Mafu, A. Dudley, S. Goyal, D. Giovannini, M. McLaren, M. J. Padgett, T. Konrad, F. Petruccione, N. Lutkenhaus, and A. Forbes, Phys. Rev. A **88**, 032305 (2013).
[9] M. Mirhosseini, O. S. Magaña-Loaiza, M. N. O’Sullivan, B. Rodenburg, M. Malik, M. P. Lavery, M. J. Padgett, D. J. Gauthier, and R. W. Boyd, New J. Phys. **17**, 033033 (2015).
[10] Y. Yan, G. Xie, P. J. Martin, H. Huang, N. Ahmed, C. Bao, Y. Ren, Y. Cao, L. Li, Z. Zhao, A. F. Molisch, M. Tur, M. J. Padgett, and A. E. Willner, Nat. Commun. **5**, 4876 (2014).
[11] F. E. Mahmouli and S. Walker, in *2012 20th Telecommunications Forum (TELFOR)* (IEEE, New York, 2012), p. 315.
[12] J. Wang *et al.*, Nat. Photonics **6**, 488 (2012).
[13] T. Yang, S. Li, O. Xu, W. Li, and Y. Wang, Remote Sens. Lett. **9**, 343 (2018).
[14] X. Bu, Z. Zhang, X. Liang, L. Chen, H. Tang, Z. Zeng, and J. Wang, Sensors **18**, 3511 (2018).
[15] S. M. Mohammadi, L. K. Daldorff, J. E. Bergman, R. L. Karlsson, B. Thidé, K. Forozesh, T. D. Carozzi, and B. Isham, IEEE Trans. Antennas Propag. **58**, 565 (2009).
[16] G. Guo, W. Hu, and X. Du, Nat. Univ. Defense Technol-Chinese Edition **35**, 71 (2013).
[17] T. Yuan, H. Wang, Y. Cheng, and Y. Qin, Sensors **17**, 630 (2017).
[18] K. Liu, Y. Cheng, Z. Yang, H. Wang, Y. Qin, and X. Li, IEEE Antennas Wireless Propag. Lett. **14**, 711 (2014).
[19] H. Liu, Y. Cheng, Y. Qin, T. Yuan, and K. Liu, in *Eighth International Conference on Digital Image Processing (ICDIP 2016)* (International Society for Optics and Photonics, Bellingham, WA, 2016), p. 100333L.
[20] K. Liu, Y. Cheng, X. Li, Y. Qin, H. Wang, and Y. Jiang, IEEE Antennas Wireless Propag. Lett. **15**, 1873 (2016).
[21] L. Li and F. Li, Phys. Rev. E **88**, 033205 (2013).
[22] Y. Chen, S. Zheng, X. Jin, H. Chi, and X. Zhang, J. Appl. Phys. **121**, 184506 (2017).
[23] F. Tamburini, E. Mari, A. Sponselli, B. Thidé, A. Bianchini, and F. Romanato, New J. Phys. **14**, 033001 (2012).
[24] E. Stegenburgs, A. Bertoncini, A. Trichili, M. S. Alias, T. K. Ng, M.-S. Alouini, C. Liberale, and B. S. Ooi, IEEE Commun. Mag. **57**, 65 (2019).
[25] W. Y. Wei, Y. Shi, Q. W. Wu, Z. K. Meng, and Z. Q. Liu, Opt. Express **29**, 3754 (2021).
[26] A. H. Tavabi, P. Rosi, E. Rotunno, A. Roncaglia, L. Belsito, S. Frabboni, G. Pozzi, G. C. Gazzadi, P. H. Lu, R. Nijland, M. Ghosh, P. Tiemeijer, E. Karimi, R. E. Dunin-Borkowski, and V. Grillo, Phys. Rev. Lett. **126**, 094802 (2021).
[27] D. Isakov, Y. Wu, B. Allen, P. Grant, C. Stevens, and G. Gibbons, R. Soc. Open Sci. **7**, 200493 (2020).
[28] S. Guo, Z. He, and R. Chen, IEEE Access **7**, 132430 (2019).
[29] X. Song, Z. Su, J. Ma, Y. Yao, Y. Bai, Z. Zheng, X. Gao, and S. Huang, Opt. Express **29**, 23717 (2021).
[30] M. Barbuto, F. Trotta, F. Bilotti, and A. Toscano, Prog Electromagn. Res. **148**, 23 (2014).
[31] A. Tennant and B. Allen, Electron. Lett **48**, 1365 (2012).
[32] G. Rui, R. L. Nelson, and Q. Zhan, Opt. Express **20**, 18819 (2012).
[33] B. Thidé, H. Then, J. Sjöholm, K. Palmer, J. Bergman, T. D. Carozzi, Y. N. Istomin, N. H. Ibragimov, and R. Khamitova, Phys. Rev. Lett. **99**, 087701 (2007).
[34] W. Zhang and Q. H. Liu, IEEE Trans. Geosci. Remote Sens. **53**, 429 (2014).
[35] J. Zhuo, F. Han, L. Ye, Z. Yu, and Q. H. Liu, IEEE Trans. Microwave Theory Tech. **66**, 3745 (2018).
[36] K. A. Michalski and J. R. Mosig, IEEE Trans. Antennas Propag. **45**, 508 (1997).
[37] B. Liang, C. Qiu, F. Han, C. Zhu, N. Liu, H. Liu, F. Liu, G. Fang, and Q. H. Liu, IEEE Trans. Geosci. Remote Sens. **56**, 877 (2017).
[38] X. Millard and Q. H. Liu, IEEE Trans. Antennas Propag. **51**, 2393 (2003).

[39] C. Yu, M. Yuan, J. Stang, E. Bresslour, R. T. George, G. A. Ybarra, W. T. Joines, and Q. H. Liu, IEEE Trans. Microwave Theory Tech. **56**, 991 (2008).

[40] Y. Ren, X. Zhao, Z. Lin, Q. Ren, Y. Chen, Y. Liu, and H. Hu, IEEE Trans. Geosci. Remote Sens. **59**, 7086 (2020).

[41] N. Zaiping, Y. Feng, Z. Yanwen, and Z. Yerong, IEEE Trans. Geosci. Remote Sens. **38**, 1709 (2000).

[42] X. Tang, J. Li, L. Wang, F. Han, H. Liu, and Q. H. Liu, IEEE Geosci. Remote Sens. Lett. **18**, 213 (2020).

[43] J. Zhuo, L. Ye, F. Han, L. Xiong, and Q. H. Liu, IEEE Trans. Antennas Propag. **68**, 4774 (2020).